

Autophagy Sustains Pancreatic Cancer Growth through Both Cell-Autonomous and Nonautonomous Mechanisms



Annan Yang¹, Grit Herter-Sprue², Haikuo Zhang², Elaine Y. Lin³, Douglas Biancur³, Xiaoxu Wang¹, Jiehui Deng², Josephine Hai², Shenghong Yang¹, Kwok-Kin Wong^{2,4}, and Alec C. Kimmelman^{1,3}

ABSTRACT

Autophagy has been shown to be elevated in pancreatic ductal adenocarcinoma (PDAC), and its role in promoting established tumor growth has made it a promising therapeutic target. However, due to limitations of prior mouse models as well as the lack of potent and selective autophagy inhibitors, the ability to fully assess the mechanistic basis of how autophagy supports pancreatic cancer has been limited. To test the feasibility of treating PDAC using autophagy inhibition and further our understanding of the mechanisms of protumor effects of autophagy, we developed a mouse model that allowed the acute and reversible inhibition of autophagy. We observed that autophagy inhibition causes significant tumor regression in an autochthonous mouse model of PDAC. A detailed analysis of these effects indicated that the tumor regression was likely multifactorial, involving both tumor cell-intrinsic and host effects. Thus, our study supports that autophagy inhibition in PDAC may have future utility in the treatment of pancreatic cancer and illustrates the importance of assessing complex biological processes in relevant autochthonous models.

SIGNIFICANCE: This work demonstrates that autophagy is critical pancreatic tumor maintenance through tumor cell-intrinsic and -extrinsic mechanisms. These results have direct clinical relevance to ongoing clinical trials as well as drug-development initiatives. *Cancer Discov*; 8(3); 276-87. ©2018 AACR.

See related commentary by Noguera-Ortega and Amaravadi, p. 266.

INTRODUCTION

Pancreatic ductal adenocarcinoma (PDAC) has a high mortality rate, with an approximately 7% 5-year survival rate for all stages of the disease. Currently available treatments are not effective for the majority of patients, as they only modestly

extend survival (1). Given its profound lethality and resistance to available therapies, there is a dire need for new treatment approaches for PDAC.

One of the characteristic features of PDAC is the upregulation of autophagy, and it has been shown that inhibition of autophagy suppresses tumor cell growth *in vitro* and in xenograft

¹Department of Radiation Oncology, Dana-Farber Cancer Institute, Harvard Medical School, Boston, Massachusetts. ²Department of Medical Oncology, Dana-Farber Cancer Institute, Harvard Medical School, Boston, Massachusetts. ³Department of Radiation Oncology, Perlmutter Cancer Center, NYU Medical School, New York, New York. ⁴Division of Medical Oncology, Perlmutter Cancer Center, NYU Medical School, New York, New York.

Note: Supplementary data for this article are available at Cancer Discovery Online (<http://cancerdiscovery.aacrjournals.org/>).

Corresponding Authors: Alec C. Kimmelman, New York University School of Medicine, 560 First Avenue, Energy Building, 2nd Floor, Suite 254, New York, NY 10016. Phone: 646-501-8940; Fax: 646-501-8904; E-mail: Alec.Kimmelman@nyumc.org; and Kwok-Kin Wong, Division of Medical Oncology, Perlmutter Cancer Center, NYU Medical School, New York, NY 10016. Phone: 646-501-8940; E-mail: Kwok-Kin.Wong@nyumc.org

doi: 10.1158/2159-8290.CD-17-0952

©2018 American Association for Cancer Research.

models (2). In *Kras*-driven genetically engineered mouse models (GEMM) of PDAC, cells lacking autophagy were less efficient in progressing into PDAC (3, 4). Several mechanisms have been proposed for how autophagy may support tumor growth in PDAC and other tumor types, including providing metabolic fuel sources as well as to allow cancer cells to deal with a variety of stressors (5, 6). In PDAC, it has been shown that autophagy inhibition decreased proliferation and increased DNA damage and apoptosis (7). In a non-small cell lung cancer mouse model, lack of autophagy caused accumulation of dysfunctional mitochondria and dysregulation of lipid catabolism (8). Besides its impact on tumor cells directly, autophagy inhibition may have antitumor effects by modulating the tumor microenvironment (9). Indeed, a recent study from our group demonstrated a cross-talk between stromal and tumor cells in PDAC, where autophagy was required in stromal cells to secrete alanine that was taken up by tumor cells to support growth (10).

The protumorigenic role of autophagy in tumorigenesis had been studied and validated using GEMMs of multiple other tumors such as melanoma (11), breast (12), lung (13), brain (14), and prostate (15) using conditional knockouts of various autophagy genes. However, with the exception of one study in lung cancer, these have all relied on loss of autophagy during the tumorigenesis process and not acutely in the fully formed tumor (16). Moreover, the nature of these models allows only for the irreversible loss of autophagy and therefore limits questions that can be asked, such as duration of inhibition needed and reversibility of potential toxicities.

Because of autophagy's supporting role in tumor growth, it became a target of interest in cancer treatment. The drug hydroxychloroquine (HCQ) has been tested in multiple clinical trials to assess the efficacy of autophagy inhibition in PDAC and other cancers (17–20). Although HCQ does inhibit autophagy, it acts at the level of the lysosome, so it will affect additional lysosomal processes (which could actually have additional antitumor effects; ref. 21). Moreover, there are potency issues with the drug, requiring high micromolar levels to inhibit autophagy and observe antitumor effects (22, 23). Interestingly, early data support that the addition of HCQ to chemotherapy in localized PDAC increases the tumor response (24, 25).

To overcome some of these obstacles, we sought to create a model where autophagy could be acutely inhibited in a reversible fashion in a fully formed tumor. This would be akin to the therapeutic scenario, much in the way a pharmacologic inhibitor works. As selective and potent inhibitors targeted to the early phases of autophagy are still in various phases of development, we took a genetic approach to model such inhibition paradigms using a previously identified dominant-negative mutant of *Atg4B* that was reported to effectively inhibit autophagy (26). In this study, we took advantage of this dominant-negative mutant to generate an inducible mouse model of autophagy inhibition and evaluated the effectiveness of autophagy inhibition in treating PDAC, as well as further explored the mechanisms of autophagy in supporting tumor growth. Indeed, we demonstrated striking tumor responses in a treatment-refractory PDAC GEMM, including some complete responses. Importantly, the innovative design of the model allowed us to demonstrate that autophagy inhibition suppresses tumor growth via tumor cell-intrinsic as well as -extrinsic factors.

RESULTS

Generating an Inducible Mouse Model of Autophagy Inhibition

Autophagy is a multistage process, and the formation of the autophagosome is an essential step to package different cargo for autophagic degradation. To form the autophagosome membrane, a cysteine protease, ATG4B, is required to conjugate LC3 with phosphatidylethanolamine and delipidate LC3-II after lysosome degradation. An enzymatically inactive mutant, ATG4B^{C74A}, was previously found to be able to sequester free LC3 *in vitro* and therefore act as a dominant-negative inhibitor of autophagy degradation (26). We developed a transgenic mouse line that carries the mSt-*Atg4B*^{C74A} gene under the control of TetOn cassette (hereafter referred to as ATG4B^{CA}; Supplementary Fig. S1). The dominant-negative ATG4B^{C74A} mutant was fused with an mStrawberry (mSt) fluorescent marker, allowing its expression to be easily tracked. The reverse tetracycline-controlled transactivator (rtTA) at the *Rosa26* locus was preceded by a stopper cassette allowing the expression to be controlled via cre-recombinase. Therefore, the combination of TetOn and LoxP expression systems allowed the expression of ATG4B^{C74A} to be temporally controlled and spatially restricted (Fig. 1A).

We crossed the *Atg4B*^{CA} [either one (+) or two (++) copies]; *Rosa-rtTA*^{LSL} transgenic mouse to a well-established pancreatic cancer GEMM: *LSL-Kras*^{G12D}, *Trp53*^{lox/+}, *p48Cre*⁺. To determine the efficiency of autophagy inhibition, we first generated cell lines derived from tumors to assess the ability of the ATG4B^{CA} to inhibit autophagic flux *in vitro*. As shown in Fig. 1B, treatment of cells with doxycycline (Dox) resulted in expression of the ATG4B^{CA} as indicated by the mStrawberry fluorescence. Expression of the ATG4B^{CA} inhibited autophagy as shown by decreased LC3 puncta, with two copies (++) showing even more potent inhibition with greater loss of puncta (Fig. 1C and D). These results were confirmed by Western blotting showing an accumulation of the nonlipidated LC3-I bands upon expression of the ATG4B^{CA} and a decrease of the LC3II band, as well as an accumulation of the cargo receptor P62 (Supplementary Fig. S2A and S2C). As expected, longer Dox treatment induced greater levels of the ATG4B^{CA} expression and showed more autophagy inhibition (Fig. 1E and Supplementary Fig. S2A).

We next tested the tight regulation of ATG4B^{CA} expression by showing dependence on the required alleles and the presence of Dox (Fig. 1F). In contrast to the control groups, the two test groups treated with Dox, ATG4B^{CA+} and ATG4B^{CA++}, which were expected to express the *Atg4B*^{CA} allele, stained positive for mStrawberry (Fig. 1F). Consistent with the *in vitro* data, potent autophagy inhibition by expression of ATG4B^{CA} was confirmed *in vivo*. LC3 puncta were present in the two control groups (not expressing ATG4B^{CA}), but were absent in the two ATG4B^{CA}-expressing groups, where the staining pattern was diffuse in nature (Fig. 1G). Autophagy cargo receptors NBR1 and P62 accumulated, forming aggregates in ATG4B^{CA++}-expressing tumors as well as normal pancreas, indicating an inhibition of autophagic flux (Supplementary Fig. S2B–S2D). We also examined autophagosome formation at the ultrastructural level by electron microscopy. As shown in Fig. 1H, most double membrane vesicular structures were closed in ATG4B⁻ tumor samples, whereas a significantly increased number of open double

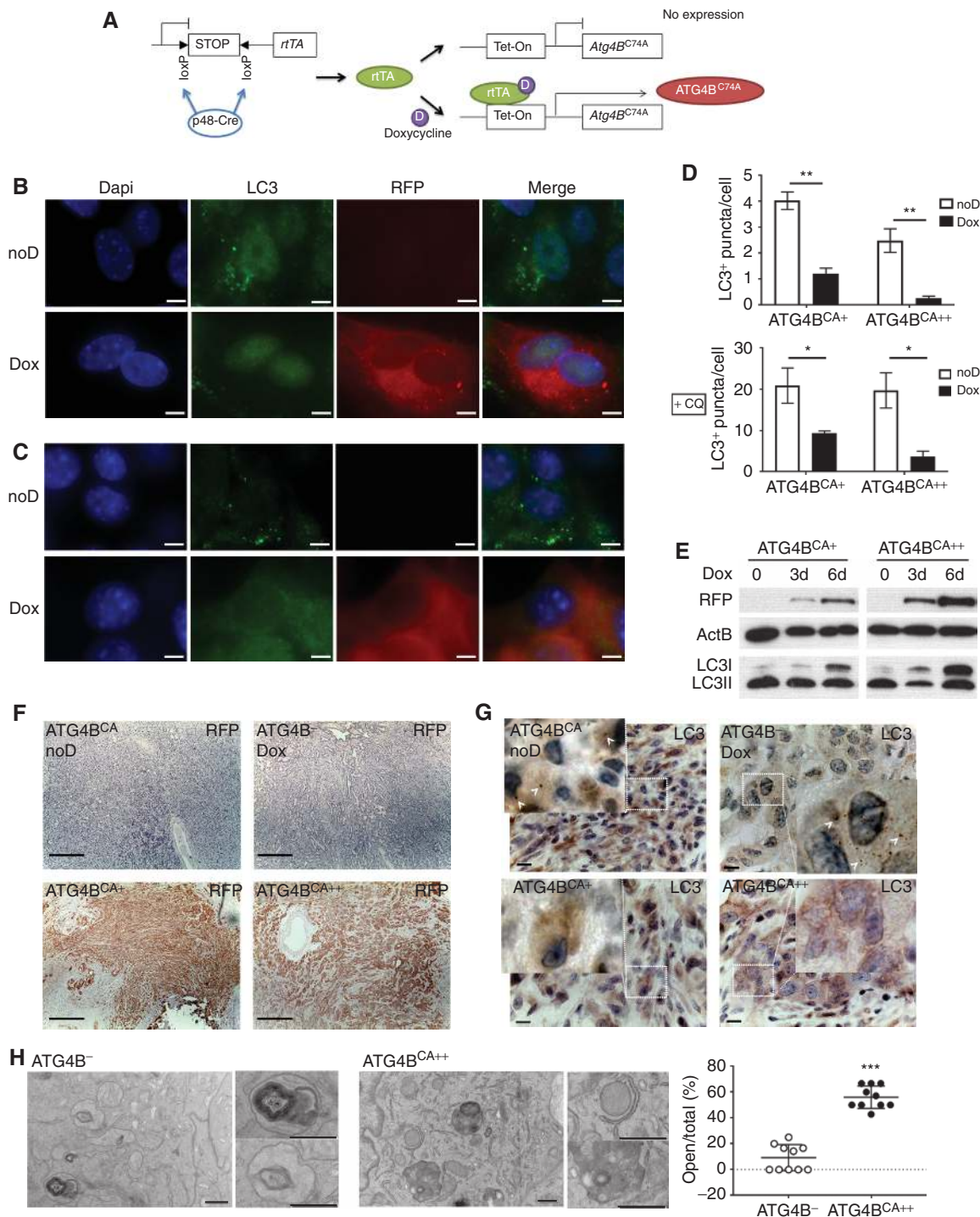


Figure 1. Generation and functional analysis of the inducible ATG4B^{CA} mouse model. **A**, Tissue-specific promoter-driven Cre expression will remove STOP cassette to express reverse rtTA. Dox binds rtTA to turn on Tet-On cassette and induce ATG4B^{C74A} expression. **B**, IF staining of LC3 (green) and RFP (red) in ATG4B^{CA+} tumor cells treated with or without Dox for 6 days. noD indicates no Dox treatment. Blue, DAPI-stained nuclei. Scale bars, 5 μ m. **C**, Representative immunofluorescence staining of LC3 and RFP in ATG4B^{CA+} and ATG4B^{CA++} tumor cells showing level of autophagy. Scale bars, 5 μ m. **D**, Quantification of LC3⁺ puncta per cell in ATG4B^{CA+} and ATG4B^{CA++} tumor cells. Dox treatment reduced autophagy level in basal (top) or chloroquine-treated (+CQ at bottom plot) condition indicating inhibited autophagic flux. More than 10 fields per cell line were measured. SD plotted as error bars. *, $P < 0.05$; **, $P < 0.001$ by *t* test. **E**, Western blot showing expression of RFP and LC3I/II in ATG4B^{CA+} and ATG4B^{CA++} cells treated with Dox for 3 days (3d) and 6 days (6d). **F**, Representative IHC images of PDACs stained for RFP with no (top), one-copy (bottom left), and two-copy (bottom right) expressions of ATG4B^{CA}. Scale bars, 500 μ m. **G**, Representative IHC images of PDACs stained for LC3 with no (top), one copy (bottom left), and two copies (bottom right) of ATG4B^{CA} expression. Inserts are 3-fold enlargement of the white framed areas; autophagosomes (LC3⁺ puncta) are marked by white arrowhead. Scale bars, 10 μ m. **H**, Electron microscope pictures showing ultrastructure of tumors from ATG4B⁻ and ATG4B^{CA++} tumors. Two samples of each genotype were examined, and a total of 10 fields were measured in the graph. ***, $P < 0.001$ by *t* test. Scale bars, 500 nm.

membrane vesicular structures were present in ATG4B^{CA++} tumors indicating a failure of completion of autophagosome formation. This observation of increased ratio of open to total autophagic structures was consistent with *in vitro* characterization of this dominant negative as previously reported (26).

Last, the ATG4B^{CA}-mediated inhibition of autophagy could be reversed by removal of Dox as shown in ATG4B^{CA++} cells (Supplementary Fig. S2E). Consistent with the ability to reversibly regulate autophagy inhibition *in vitro*, expression of mStrawberry was reduced after removal of Dox in ATG4B^{CA++} tumors *in vivo* (Supplementary Fig. S2F).

Inhibition of Autophagy Decreases Growth of Fully Formed PDAC

To evaluate the effect of autophagy inhibition on tumor growth, we used high-resolution ultrasound imaging to identify PDACs and follow their growth (Supplementary Fig. S3A). We generated four groups of mice that did not express ATG4B^{CA} due to lack of the genetic alleles or Dox exposure. The four negative control cohorts of mice did not express ATG4B^{CA} and showed no significant differences in tumor growth or tumor-specific survival (Supplementary Fig. S3B and S3C). Thus, for comparison, we combined all mice not expressing ATG4B^{CA} in one group denoted as ATG4B⁻ from here forward. To study how autophagy inhibition affected established PDAC growth, we first allowed tumors to form and measured volume by serial high-resolution ultrasound. During the study, we did not observe significant effect of Dox food or autophagy inhibition on weight of tumor-bearing mice (Supplementary Fig. S3D and S3E). Compared with controls, the ATG4B^{CA+} (*Atg4B^{CA+}, Trp53^{lox/+}, LSL-Kras^{G12D}, Rosa-rtTA^{LSL}, p48Cre⁺*) group showed slower tumor growth kinetics and extended tumor-specific survival (Fig. 2A and B). However, after an initial delay in tumor progression, all tumors resumed growth and mice finally succumbed to tumor burden. An assessment of these tumors at endpoint revealed that all mice ($n = 10$) at the end of the study had lost expression of the ATG4B^{CA} to various degrees, with 5 of 10 tumors showing nearly complete loss of ATG4B^{CA} expression (Supplementary Fig. S4A). Once tumor cells lost ATG4B^{CA} expression, autophagosome formation resumed consistent with silencing of the ATG4B^{CA} allele or outgrowth of cells that did not express ATG4B^{CA} (Supplementary Fig. S4B). To test this hypothesis, we assessed a cohort of tumor-bearing mice at serial time-points for ATG4B^{CA} expression after starting Dox and observed a gradual loss of ATG4B^{CA} expression over time (Supplementary Fig. S4C). Furthermore, primary cell lines harvested from tumors showed loss of the ATG4B^{CA} allele in four of five tumors (Supplementary Fig. S4D and S4E).

To examine if there was a dose-response effect of autophagy inhibition, we next analyzed tumor growth and survival in mice with two copies of the ATG4B^{CA} (ATG4B^{CA++}). Strikingly, this cohort showed a more significant antitumor response, with 6 of 10 tumors showing frank regression after 4 days of Dox treatment, and 3 of these 6 mice maintained inhibited growth with less than doubling of the initial tumor volume after 2 weeks of treatment (Fig. 2C). However, despite these dramatic responses, there was no significant increase in survival in the ATG4B^{CA++} group compared with the control group (Fig. 2D). After examining the ATG4B^{CA++} tumors at endpoint, we found

that all 4 mice that had died within 3 weeks showed histologic disruption of the normal pancreas architecture with significant areas of metaplasia, which were composed of abnormal ductal-like, mucin-rich cells stained positive for CK19 (Supplementary Fig. S5A). In addition, the pancreata showed loss of β -islets in both the ATG4B^{CA++} and control mice likely due to tumor replacement of normal pancreata (Supplementary Fig. S5B). Serum insulin levels were not significantly changed in ATG4B^{CA++} mice compared with ATG4B⁻ mice, indicating there was not likely frank diabetes. Consistent with this, there was only minimal expression of ATG4B^{CA++} in the β -islets (Supplementary Fig. S5B) due to differences in expression of the allele between the tissues. We further stained for amylase and found a dramatic loss of normal acinar cells, indicating a profound disruption of the exocrine pancreas in the *Atg4B^{CA++}*-expressing tumor-bearing mice (Supplementary Fig. S5C). To further understand the correlation of autophagy inhibition, loss of acinar cells, and metaplasia, we examined the histology of pancreata of non-tumor-bearing *Atg4B^{CA++}, Trp53^{lox/+}, Rosa-rtTA^{LSL}, p48Cre⁺* mice. After over 40 weeks on Dox diet to induce ATG4B^{CA} expression, there was no loss of acinar cells, metaplasia, or ductal transformation (Supplementary Fig. S5D). Thus, we concluded that this metaplastic phenotype was likely due to the nature of the transgenic model, where all cells of the pancreas express oncogenic *Kras^{G12D}* and were consistent with our previous studies showing that inhibition of autophagy predisposes mutant KRAS-expressing mice to acinar-ductal metaplasia (benign tumor initiation; ref. 4).

Because our model allows the reversible inhibition of autophagy, we sought to understand whether intermittent inhibition would also be effective in inhibiting PDAC growth, similar to the way chemotherapy is often given on a periodic basis. In this regard, we fed mice with Dox for a week and then placed them back on normal chow for a week. This was repeated for multiple cycles, and tumor response was monitored by ultrasound. With this intermittent treatment, only 2 of the 11 mice succumbed to the metaplasia-related death as those observed in ATG4B^{CA++} continuous treatment group. Impressively, 36% of mice (4 of 11) had a significant sustained response (less than doubling initial tumor volume) that was maintained for up to 15.5 weeks. Seven of 11 mice had significant responses at the first week, then tumors resumed growth in the off-Dox cycle, and eventually mice met protocol endpoint. There was no difference in tumor size at detection between the subgroup of mice with the sustained responses to the autophagy inhibition ($n = 4$) and the rest of the mice ($n = 7$; Supplementary Fig. S5D). Overall, this intermittently treated cohort showed significant tumor growth delay, which resulted in an increased survival, compared with the control group (Fig. 2C and D). Consistent with the improved response, most of the tumor cells retained expression of ATG4B^{CA} when harvested at the end of Dox cycle (Supplementary Fig. S2F), and PCR of all ATG4B^{CA++} tumor cell lines confirmed their maintenance of the ATG4B^{CA} allele (Supplementary Fig. S4D).

Despite the varied individual long-term response to autophagy inhibition, all tumors in ATG4B^{CA++} groups responded within a week after Dox treatment initiation either by regression or by stable disease (Fig. 2E). We defined a tumor as regressing if the relative growth compared with detection volume was less than 1, indicating that the volume had decreased compared with

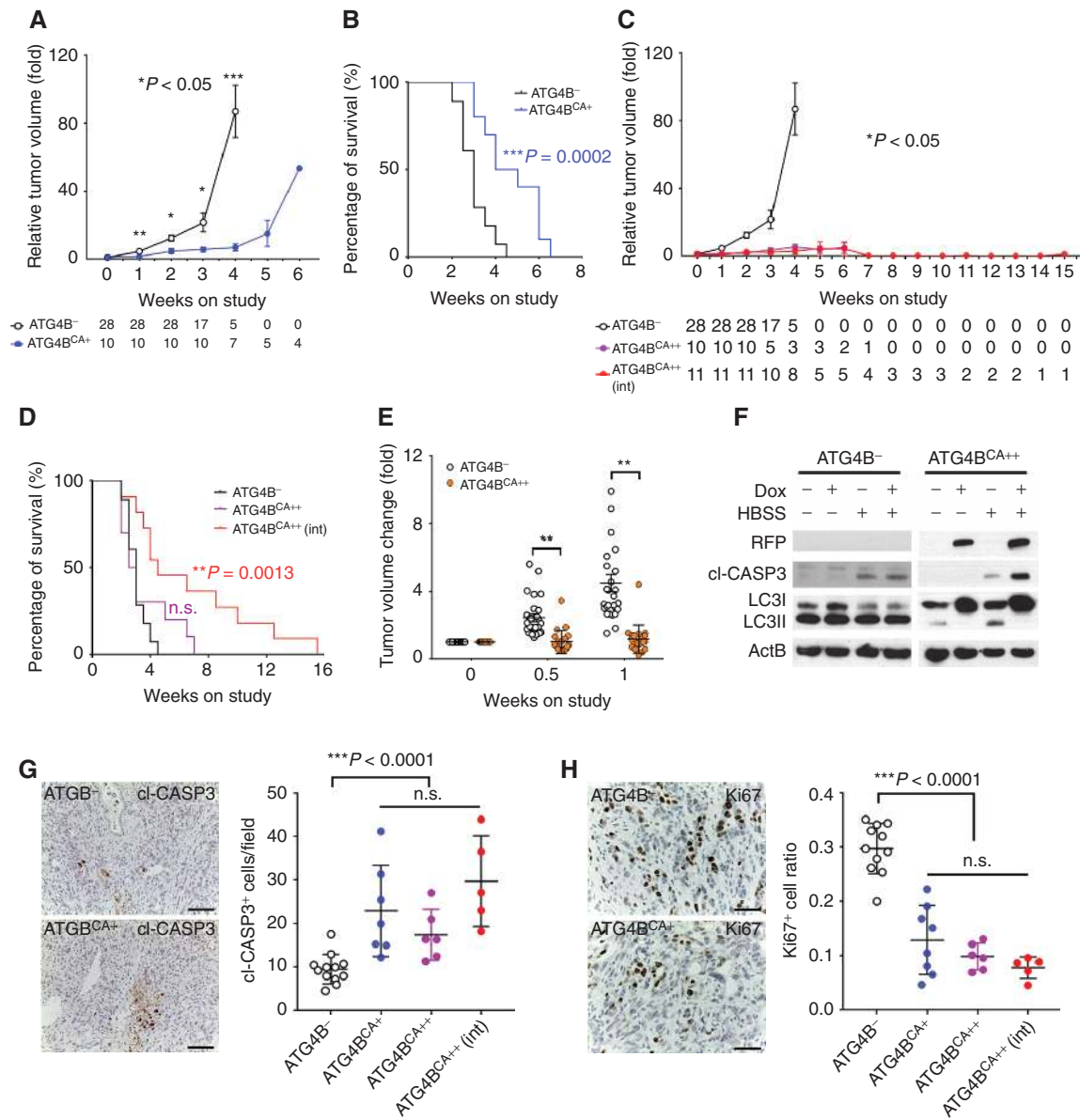


Figure 2. Impact of autophagy inhibition on PDAC growth in ATG4B^{CA+} and ATG4B^{CA++} mice. **A**, Comparison of tumor growth between ATG4B⁻ control and ATG4B^{CA+} mice. Tumor volumes were measured by ultrasound, and relative growth was plotted against time (weeks) since initial tumor identification (0 wk), and Dox diet (625 mg/kg Dox) was given after tumor identification. Numbers of mice in each group at each time-point are indicated in the graph. **B**, Survival analysis of mice plotted in **A**. P value by the Log-rank test. **C**, Comparison of tumor growth among ATG4B⁻ control, ATG4B^{CA++}, and ATG4B^{CA++} intermittently induced (Int) groups. Tumor volumes were measured by ultrasound, and relative growth was plotted against time (weeks) from initial tumor identification (0 wk). Numbers of mice in each group at each time-point are indicated in the graph. **D**, Survival analysis of mice plotted in **C**. P value by the log-rank test. **E**, Relative growth comparison between ATG4B⁻ ($n = 28$) and ATG4B^{CA++} ($n = 21$) tumors after Dox treatment for 1 week. **, $P < 0.001$ by t test. **F**, Western blot of RFP, cleaved Caspase-3, and LC3I/II in starved [treated with Hank's Balanced Salt Solution (HBSS)] ATG4B⁻ and ATG4B^{CA++} tumor cells treated with or without Dox. **G**, IHC analysis of cleaved Caspase-3 staining in ATG4B⁻ and ATG4B^{CA+} tumors. Scale bar, 100 μ m. Cleaved Caspase-3⁺ cells/field were compared as shown in the right plot. Each dot represents one mouse with more than 5 fields measured per mouse. **H**, IHC analysis of Ki67 staining in ATG4B⁻ and ATG4B^{CA+} tumors. Scale bar, 50 μ m. Proliferation index as Ki67⁺ cell ratio was compared as shown in the right plot. Each dot represents one mouse with more than 5 fields measured per mouse.

the initial size. After 1 week, 0 of 28 mice in the control group, compared with 7 of 21 ATG4B^{CA++} mice, showed regression ($P = 0.0014$ by Fisher exact test). To measure if ATG4B^{CA} expression alone could induce apoptosis, we used ATG4B^{CA++} primary cell lines and found no cleaved Caspase-3 expression under normal culture condition with 10% FBS. However, if we starved cells with Hank's Balanced Salt Solution (HBSS), we observed

increased cleaved Caspase-3 expression in ATG4B^{CA}-expressing cells (Fig. 2F). This suggested that blocking autophagy under nutrient-restricted circumstances sensitized cells to death and was consistent with the fact that more apoptosis was seen *in vivo* next to areas of necrosis (suggesting they were poorly perfused and nutrient deprived). Both single-copy (ATG4B^{CA+}) and two-copy (ATG4B^{CA++}) tumors showed increased apoptosis compared

with controls (Fig. 2G). We then analyzed proliferation in tumors by measuring Ki67 expression. Consistent with the decreased growth, we found there was a significant reduction of proliferating cells in ATG4B^{CA+} and ATG4B^{CA++} groups (Fig. 2H).

Using a KRAS-driven lung GEMM, we were able to extend these findings to lung cancer by monitoring tumor growth with MRI (Supplementary Fig. S6A). Once tumor was identified, mice were randomly assigned to Dox diet as in the PDAC studies. Similar to the PDAC model, we noticed a significant growth deficit in ATG4B^{CA+} mice (Supplementary Fig. S6B). ATG4B^{CA+} tumors showed fewer Ki67⁺ cells compared with ATG4B⁻ tumors, indicating less proliferation (Supplementary Fig. S6C). However, unlike PDAC, lung tumors did not show significant increases in apoptosis. This may reflect the unique PDAC microenvironment which is known to be poorly perfused, hypoxic, and nutrient poor (27).

Cell-Intrinsic and -Extrinsic Factors Affect Tumor Growth in Response to Autophagy Inhibition

Previous work from our group has shown in various systems that autophagy supports PDAC tumor cell growth through effects on the tumor cell itself (2). More recently, we identified that autophagy in the stromal compartment was critical for a metabolic cross-talk to fuel tumor cells (10). Therefore, we set out to explore the contributions of autophagy to various aspects of tumor growth, taking advantage of the unique features of the ATG4B^{CA} model. Consistent with previous findings of autophagy inhibition in PDAC, tumor-derived cell lines from the ATG4B^{CA++} model showed reduced clonogenic growth as well as significantly decreased growth in soft agar (Fig. 3A and B). To confirm the cell-autonomous effects of autophagy inhibition, we performed xenograft studies where we implanted ATG4B⁻ cells in the left flank and ATG4B^{CA++} cells in the right flank of the same nude mice. After allowing tumors to form, we then randomized mice to a normal or a Dox diet and compared the growth rates of ATG4B^{CA++} with ATG4B⁻. Consistent with the *in vitro* data, autophagy inhibition decreased the tumor growth kinetics (Fig. 3C, Supplementary Fig. S7). However, in contrast to the autochthonous model, there were no tumor regressions. Similarly, orthotopic injections of ATG4B^{CA++} cells into the pancreata of nude mice showed significantly decreased growth kinetics, but again no regressions (Fig. 3D). The more profound responses seen in the autochthonous model suggested that certain aspects of this model were influencing the response of the tumor, such as the more accurate modeling of the tumor microenvironment. Consistent with this idea, it appeared that the inflammatory infiltrate was more robust in autochthonous tumors expressing the ATG4B^{CA} (Supplementary Fig. S8A). As an initial characterization, we performed IHC to assess for various immune cell populations. Although we did not observe any differences in the presence of intratumoral T cells (Supplementary Fig. S8A), the ATG4B^{CA++} tumors had significantly more CD68⁺ macrophages present (Fig. 3E). To confirm these findings, we assessed for the presence of macrophages in the tumors of ATG4B⁻ and ATG4B^{CA++} mice using flow cytometry as well as immunofluorescence (IF) staining with another marker, F4/80 (Supplementary Fig. S8B). This again demonstrated a significant increase in macrophages in the ATG4B^{CA++} tumors. In contrast

to the autochthonous model, we found there was no increase of macrophages in ATG4B^{CA++} tumors grown in nude mice (Fig. 3F). We performed some initial characterization of the macrophage subtype of the tumor-infiltrating macrophages. We used iNOS (which often represents antitumor, proinflammatory macrophages) and ARG1 (often enriched in protumor macrophages). Interestingly, we found both iNOS⁺ and ARG1⁺ macrophage populations were increased in ATG4B^{CA++} tumors, indicating that multiple macrophage populations infiltrate the tumor (Supplementary Fig. S8C and S8D).

The increase of intratumoral macrophages could be a cause of either the increased tumor response to autophagy inhibition seen in the autochthonous model or merely a consequence of attempting to clear increased numbers of dying tumor cells. To determine if the macrophages were influencing tumor response to autophagy inhibition, we depleted macrophages using liposomal clodronate (28) and assessed the efficacy of ATG4B^{CA++} expression as compared with mice treated with a control PBS liposomal solution. We first demonstrated that the clodronate significantly impaired the increased macrophage infiltration seen in the ATG4B^{CA++} tumors (ref. 28; Supplementary Fig. S8E). Strikingly, depletion of macrophages markedly impaired the response of tumors to autophagy inhibition (Fig. 3G) while having no significant effect on ATG4B⁻ tumor growth (Supplementary Fig. S8F). Taken together, these data demonstrated that autophagy inhibition in PDAC cells has direct effects on tumor cell growth, but macrophage-mediated mechanisms are also involved in the antitumor response.

Stromal Autophagy and PDAC Growth

We had previously demonstrated through coculture and coinjection studies that autophagy inhibition in the stroma can influence growth of the PDAC tumor cells through the secretion of amino acids (10). The design of the ATG4B^{CA} system would allow us to test this in a more sophisticated fashion. We first bred *Atg4B^{CA}, Rosa-rtTA^{LSL}* mice to *Ubc-ERT/Cre⁺* mice that express Cre-recombinase in all tissues after exposure to tamoxifen. After 5 days of tamoxifen injections followed by a week on Dox diet, most major tissues from *Atg4B^{CA}, Rosa-rtTA^{LSL}, Ubc-ERT/Cre⁺* mice had expression of ATG4B^{CA}, and this expression lasted until harvest at 52 weeks. Due to the limitation of *Col1A* knockin locus where *mSt-Atg4B^{C74A}* cDNA was integrated, there was no expression of ATG4B^{CA} in brain or muscle, and expression in most other tissues was mosaic in nature consistent with previous report (ref. 29; Supplementary Fig. S9A). Thus, we did not observe any behavior abnormalities or premature death as had been reported in the *Atg7* adult knockout mice (Supplementary Fig. S9B). There was only one mouse from the ATG4B^{CA++} group that died earlier than 30 weeks, due to a hernia. Based on the hematoxylin and eosin histology examination of all mice older than 52 weeks, no significant difference was found among all groups. Overall, in this model, the whole-body inhibition of autophagy in a mosaic fashion did not appear to have any grossly detrimental effect on normal organs.

Next, we wanted to distinguish the cell-autonomous effect versus non-cell-autonomous effects of autophagy inhibition on tumor seeding efficiency and growth. We used mouse tumor cell lines harvested from primary tumors and performed

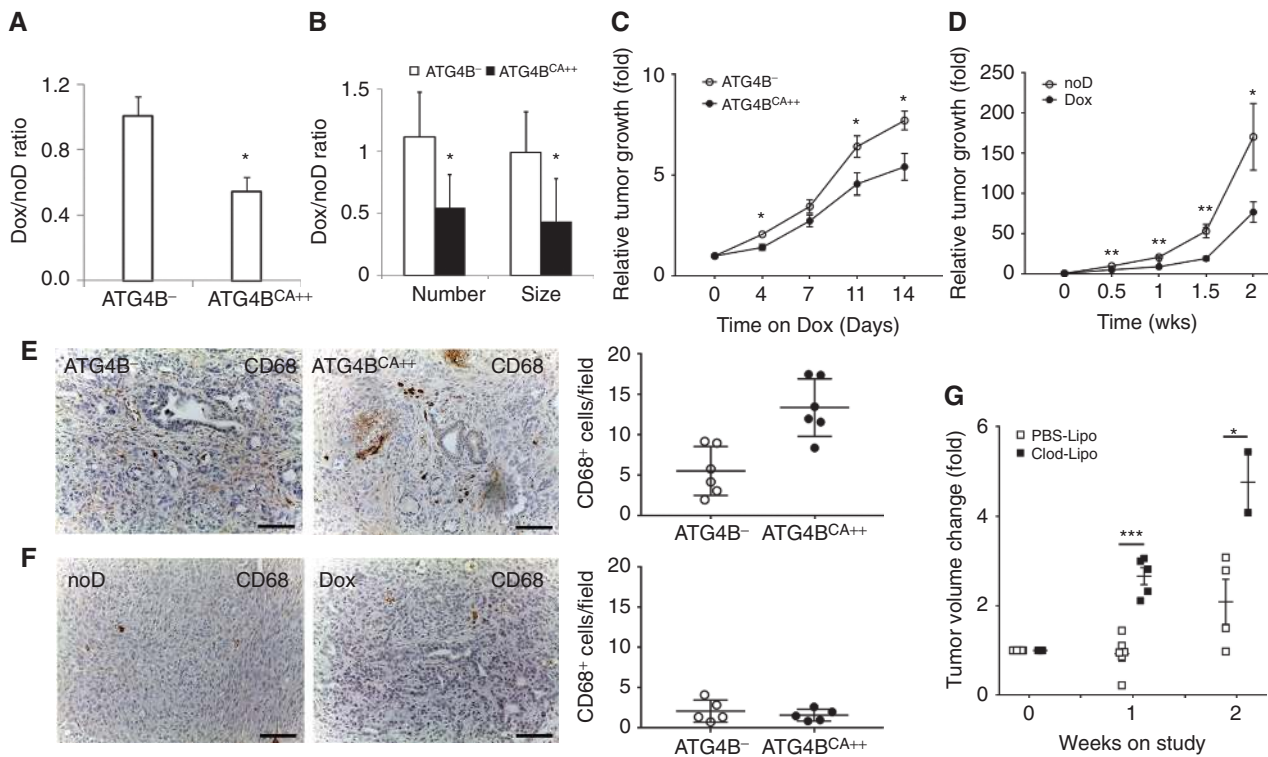


Figure 3. The cell-intrinsic and cell-extrinsic effect of autophagy inhibition on tumor growth. **A**, Plot of colony number (mean + SD) formed in ATG4B⁻ and ATG4B^{CA++} cells. Each group contained 3 individual cell lines, and each cell line was repeated 3 times. *, $P < 0.05$ by t test. **B**, Plot of colony number and size formed in ATG4B⁻ and ATG4B^{CA++} cells grown in soft agar. Each group contained 3 individual cell lines, and each cell line was repeated 3 times. *, $P < 0.05$ by t test. **C**, Relative growth of ATG4B^{CA++} and ATG4B⁻ subcutaneous xenografts on Dox diet ($n = 10$ in each group; *, $P < 0.05$). **D**, Relative growth of orthotopic pancreatic tumors (*, $P < 0.05$; ***, $P < 0.0001$). **E**, Representative images of CD68 IHC in ATG4B⁻ and ATG4B^{CA++} autochthonous tumors showing macrophage infiltration. Scale bar, 100 μ m. Quantification of CD68⁺ cells per field showed significantly increased number of macrophages in the ATG4B^{CA++} group ($n = 6$) vs. ATG4B⁻ group ($n = 6$), and 5 to 10 randomly selected fields were quantified for each tumor (**, $P = 0.0021$ by t test). **F**, Representative images of CD68 IHC in ATG4B^{CA++} tumors orthotopically injected in nude mice either on or off Dox food. Scale bar, 100 μ m. There was no significant difference in macrophage infiltration between the ATG4B^{CA++} ($n = 5$) group and the ATG4B⁻ group ($n = 5$), and 8 fields were randomly selected for each tumor. **G**, Relative growth of ATG4B^{CA++} tumors treated with empty liposome (PBS-Lipo; $n = 6$) or clodronate liposome (Clod-Lipo; $n = 5$). *, $P < 0.05$; ***, $P < 0.001$ by t test.

orthotopic injection into MHC H2-matched hosts (50% B6 and 50% FVB/N). First, we injected ATG4B^{CA++} tumors into ATG4B^{CA++} mice or ATG4B⁻ mice on normal or Dox diets as shown in Fig. 4A. Three groups of mice were generated to allow a pairwise comparison on the effect of autophagy inhibition in tumor cells or whole body: ATG4B⁻ tumors in ATG4B⁻ mice (BD⁻ TU⁻, $n = 13$), ATG4B^{CA++} tumors in ATG4B⁻ mice (BD⁻ TU⁺, $n = 11$), and ATG4B^{CA++} tumors in ATG4B⁺ mice (BD⁺ TU⁺, $n = 16$). After 3 weeks, both groups that had ATG4B^{CA++} expressed in the tumor (either BD⁻ or BD⁺) showed significant difference in the development of tumors compared with the group where there was no autophagy inhibition in either the tumor or whole body (BD⁻ TU⁻; Fig. 4B). These results indicate that cell-autonomous autophagy inhibition plays a major role in controlling tumor seeding efficiency. Furthermore, tumor growth rate was unaffected by the whole-body expression and was determined predominantly by cell-intrinsic expression of Atg4B^{CA++} (Fig. 4C). However, we noticed that although the ultimate ability to form tumors was determined by the expression of ATG4B^{CA} in the tumor itself, there was an early trend of delayed tumor formation in mice with whole-body expression of ATG4B^{CA++}

(Fig. 4B). Indeed, at the earliest time-points, the seeding efficiency was lowest in the BD⁺ TU⁺ group where both body and tumor cells had autophagy inhibition (Fig. 4B). To further explore the whole-body effect of autophagy inhibition on tumor take, we injected ATG4B⁻ cell lines into ATG4B^{CA++}, *Rosa-rtTA^{LSL}, Ubc-ERT/Cre⁺* mice on either normal or Dox diet (Fig. 4D). Two groups were generated to understand the non-tumor cell-autonomous effects of autophagy inhibition: ATG4B⁻ tumors in ATG4B⁻ mice (BD⁻ TU⁻, $n = 15$) and ATG4B⁻ tumors in ATG4B^{CA++} mice (BD⁺ TU⁻, $n = 16$). We found there was indeed a significantly delayed tumor take in the BD⁺ group (Fig. 4E). Once a tumor successfully established, there was no significant difference in tumor growth between ATG4B⁻ and ATG4B^{CA++} mice (Fig. 4F). Importantly, Dox alone did not affect tumor seeding (Supplementary Fig. S10A).

In line with our previous work demonstrating the importance of stellate cell autophagy in supporting tumor growth, we found a negative selection against the expression of the ATG4B^{CA} in stellate cells at the endpoint of the experiment when tumors have formed (Supplementary Fig. S10B). In contrast, the ATG4B^{CA} was expressed in stellate cells in normal pancreas (Supplementary Fig. S10C). This negative selection

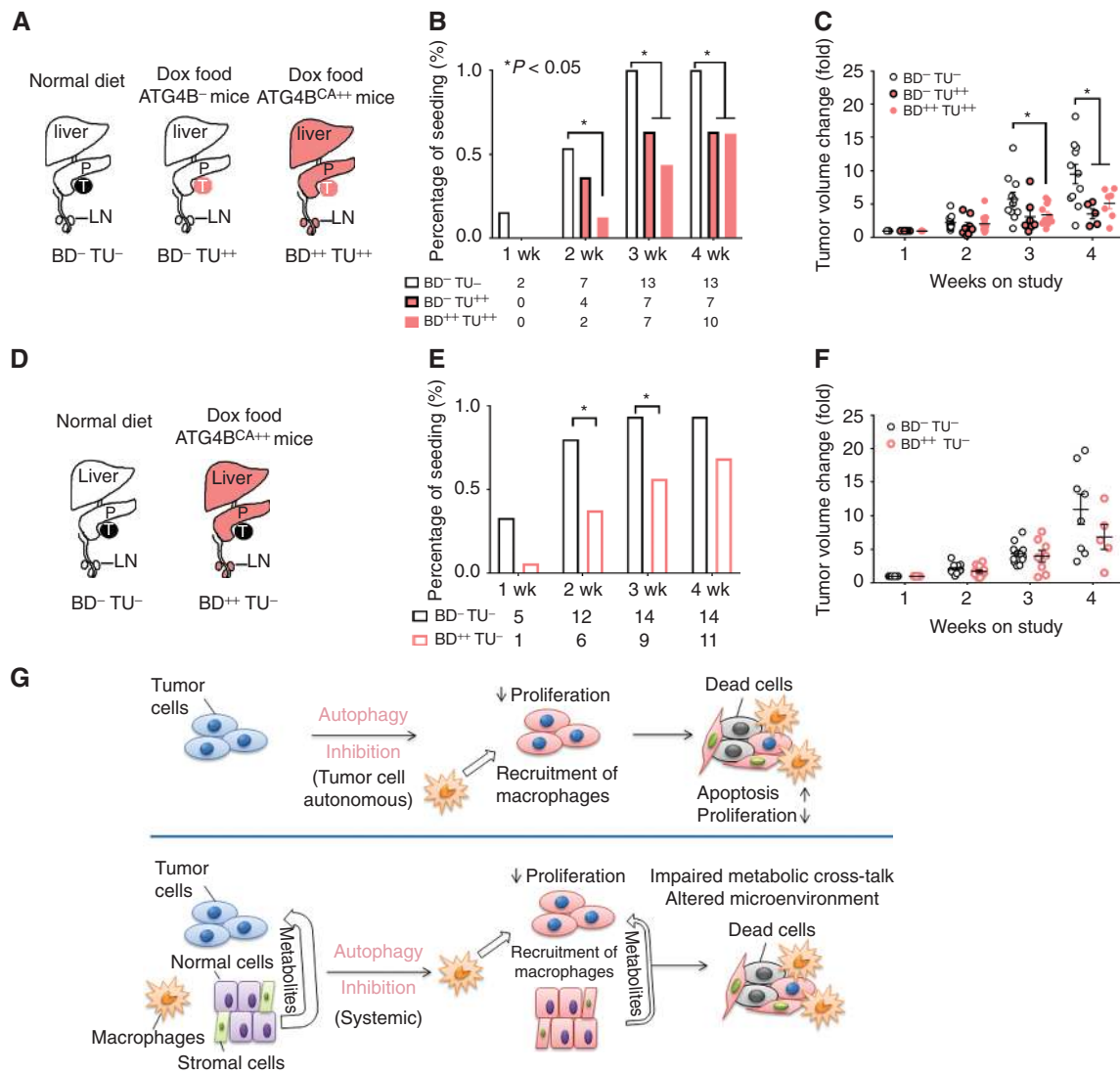


Figure 4. Autophagy inhibition impairs tumor seeding efficiency through cell-autonomous and non-cell-autonomous mechanisms. **A**, Schematic experimental design to demonstrate how tumor take was affected by autophagy inhibition. **B**, Detection of tumor take with ultrasound after orthotopic injection of ATG4B^{CA++} cells into ATG4B^{CA++}, *Rosa-rtTA^{LSL}*, *Ubc-ERT/Cre⁺* mice on normal diet (BD⁻ TU⁻, *n* = 13), ATG4B⁻Ubc⁻ mice on Dox diet (BD⁻ TU⁺⁺, *n* = 11), and ATG4B^{CA++}, *Rosa-rtTA^{LSL}*, *Ubc-ERT/Cre⁺* mice on Dox diet (BD⁺⁺ TU⁺⁺, *n* = 16). Numbers of mice with detected tumors are shown in the graph. *, *P* < 0.05 by Fisher exact test. **C**, Relative tumor growth of orthotopically injected tumors plotted in **B**. *, *P* < 0.05. **D**, Schematic of experimental design to assess the non-cell-autonomous effect of autophagy inhibition on tumor take. **E**, Detection of tumor take with ultrasound after orthotopic injection of ATG4B⁻ cells into ATG4B^{CA++}, *Rosa-rtTA^{LSL}*, *Ubc-ERT/Cre⁺* mice on normal diet (BD⁻ TU⁻, *n* = 15) and on Dox diet (BD⁺⁺ TU⁻, *n* = 16). Numbers of mice with positive seeding were shown in the graph. *, *P* < 0.05; **, *P* < 0.001 by Fisher exact test. **F**, Relative tumor growth of orthotopically injected tumors plotted in **E**. No significant differences are seen between groups at any time-points. **G**, Model of cell-autonomous and non-cell-autonomous mechanisms of autophagy inhibition affecting PDAC growth.

in the tumor supports the concept that stellate cell autophagy is important for tumor growth in the pancreas and consistent with our prior work demonstrating an autophagy-dependent metabolic cross-talk (10).

DISCUSSION

In this study, we addressed several questions regarding the inhibition of autophagy as a therapeutic target in pancreatic cancer. Although HCQ is being tested in PDAC as well as multiple other cancers and has shown some preliminary

successes (30), the drug not only inhibits autophagy but also inhibits other aspects of lysosomal scavenging. Therefore, it is not possible to specifically assess the contributions of its antiautophagy effects. In addition, there are potency issues with HCQ that may limit its utility (31). Together, these limitations require the development of more potent and specific autophagy inhibitors to rigorously test this approach in the clinic. Such inhibitors are in various phases of development.

In the interim, the inducible ATG4B^{CA} model allowed us to address several fundamental questions that are critical to optimally bring autophagy inhibition forward to the clinic. First, it

allowed us to model the impact of potent inhibition at the early part of the autophagic process in fully formed tumors. Second, the inducible nature of the model allowed us to test the impact of intermittent autophagy inhibition. In essence, we have been able to utilize this new model to create a “genetic drug.” Combining this model with a pancreatic cancer GEMM, we have shown that these tumors show robust responses to autophagy inhibition. Indeed, our data also suggest that intermittent dosing of future autophagy inhibitors could be a viable strategy to create a therapeutic index. Although the mosaic nature of the model limited our ability to assess toxicity of whole-body inhibition of autophagy, the lack of observed toxicity and histologic damage of tissues suggests that autophagy inhibitors may be tolerated by patients when dosed appropriately. It is important to note that the ATG4B^{CA} transgenes did not express in the central nervous system (CNS), which may also explain the lack of toxicity in our model, as CNS toxicity is a major cause of morbidity in previous studies (16). Given the relative ease of designing small molecules that cannot cross the blood-brain barrier (BBB), future autophagy inhibitors may be designed with favorable toxicity profiles. Such an approach was taken with newly designed glutaminase inhibitors (32), where the known CNS toxicity was mitigated by limiting BBB penetration.

Using this new model, we have also been able to address some debated biological questions regarding the role of autophagy in pancreatic cancer. In particular, it has allowed us to deconvolute the cell-autonomous (affects the tumor cell directly) and non-cell-autonomous (affects tumor growth through its role on other cell types), and shows that both are relevant to its role in tumor promotion (Fig. 4G). Similar to what we have previously shown, autophagy inhibition in the context of tumor-initiating mutations (*Kras* mutation and *Trp53* loss) can predispose to metaplasia and premalignant lesions (PanIN). This is highlighted in the genetic model where the entire pancreas has these oncogenic and tumor-suppressor mutations, a situation that would not occur in the context of the human disease. Indeed, we do not see these marked histologic changes in the context of autophagy inhibition in pancreata where oncogenic KRAS is not expressed. Therefore, we believe that this will not likely be a significant issue in the therapeutic situation in patients where these genetic lesions are restricted to neoplastic tissue. Although this “model effect” is not likely a concern for therapy (treating patients with established cancer), it might suggest that using autophagy inhibitors chronically as a chemopreventive strategy could be an issue.

One of the novel findings in this study was that the impact on tumor regression, when autophagy was inhibited in the tumor itself, was partially mediated by macrophages. Indeed, we could significantly inhibit the responses to the ATG4B^{CA} by depleting macrophages in the mouse. As macrophage modulation is being tested in PDAC as a therapeutic approach (28, 33), whether combining such agents with autophagy inhibitors would be beneficial remains to be determined. We speculate that autophagy could regulate macrophage infiltration by degradation of inflammation regulators, as well as by directly affecting cytokine secretion as has been shown previously (34). The fact that autophagy inhibition systemically affects tumor engraftment supports the additional contribution of non-cell-autonomous effects in the

efficacy of autophagy inhibition. One likely explanation for this effect is the autophagy-dependent metabolic cross-talk between the tumor cells and the stroma previously described by our group. However, we cannot rule out the contribution of other systemic effects of autophagy inhibition, such as potentially heightened immune surveillance as an example. However, the fact that there appear to be stromal and immunologic mediators that contribute to the antitumor effects of autophagy inhibition further supports both a cell-autonomous and non-cell-autonomous protumorigenic role for autophagy in PDAC and provides the strongest evidence to date that acute and potent inhibition of autophagy is effective in treating this disease in mouse models. One limitation of the study is that we have not yet assessed the impact of autophagy inhibition in different host cell types in the PDAC microenvironment other than stellate cells (10). Future studies will define the broader role of autophagy in distinct cell populations and how these influence tumor growth. Finally, future studies will develop rationally designed therapeutic combinations with autophagy inhibition to guide trials with newer autophagy inhibitors.

METHODS

Construction of Targeting Vector and Screening of ES Cells

The mStrawberry-ATG4B^{C74A} cDNA fragment was cloned from the mStrawberry-ATG4B^{C74A} plasmid generously gifted by Dr. Tamotsu Yoshimori (Addgene plasmid # 21076, Osaka University, Suita, Osaka; ref. 26), and into pCol-TGM that was a gift from Scott Lowe (Addgene plasmid # 32715; ref. 35). The pBS31-mStrawberry-ATG4B^{C74A} targeting vectors were co-electroporated into C2 mouse embryonic stem cells (Thermo Scientific Open Biosystems; #MES4305) with a plasmid expressing FLPE recombinase (pCAGGS-FlpE; Thermo Scientific Open Biosystems; #MES4488) as previously described (29). ES cells were screened for integration of the transgene by PCR, and correctly targeted ES cells were injected into C57BL/6 blastocysts. Chimeras were crossed to the FVB/NJ inbred mice (The Jackson Laboratory; ME #001800). The *Atg4B*^{C74A} mice are available at The Jackson Laboratory as Stock No. 031540.

Mice

All mice used in this study were housed in the pathogen-free animal facilities in Dana-Farber Cancer Institute (Boston, MA). All procedures were approved by the Dana-Farber Animal Care and Use Committee (Protocol number: 10-055) and carried out in strict accordance with the recommendations in the Guide for the Care and Use of Laboratory Animals of the National Institutes of Health. In *Rosa-rtTA*^{LSL} mice, the Dox-responsive rtTA is knocked into the transcriptional start site at the ubiquitously expressed *Rosa26* locus and is preceded by a lox-stop-lox (LSL) cassette (36). PDAC mice contained *Kras*^{G12D} allele knocked into the endogenous *Kras* locus, preceded by an LSL cassette (37); *Trp53*^{lox/+} allele where lox-P sites are inserted in the intron 1 and intron 10, respectively (38); and the *p48Cre* allele that harbors a cre-recombinase gene in the endogenous *Ptfla* locus (39). *Ubc-ERT/Cre*⁺ mice (The Jackson Laboratory; ref. 40) were backcrossed to B6 background and then bred with *Atg4B*^{CA++}, *Rosa-rtTA*^{LSL} mice. All mice included in the survival analysis were euthanized when criteria for disease burden were reached or when targeted analysis endpoints were reached.

Measurement of Tumor Volume by Ultrasound

All mice were kept on a normal diet and screened weekly for tumor presence upon reaching 6 weeks of age. Once a tumor was detected, the mouse was randomly assigned to either the control group by being

kept on the normal diet or the treatment group by being switched to Dox diet (625 mg/kg Dox). Tumors were at least 2 mm in diameter prior to enrollment (volumes ranged from 4 to 80 mm³). Tumor volumes (in mm³) were measured twice a week by 3-D ultrasound imaging (VisualSonics Vevo 770). The tumor relative growth rate was measured by normalizing each tumor volume to its first measurement at detection.

Lung Cancer Model and Magnetic Resonance Imaging

Single-nodule murine lung cancer was induced by intrathoracic injection of Adeno-Cre virus (Gene Transfer Vector Core Facility at the University of Iowa) into *Kras*^{G12D} mice at the age of 6 to 8 weeks as described previously (41). Animals were randomly assigned to various treatment groups as indicated once tumors had formed. Tumor growth was evaluated every 2 weeks using MRI until the tumor burden met euthanasia criteria. Mice were imaged on a 4.7 Tesla BioSpec 47/40 MRI scanner (Bruker BioSpin). Animals were anesthetized with 1% to 3% isoflurane via a nose cone. A gradient echo flow compensated sequence using a repetition time of 372.5 ms, echo time of 7.0 ms, and flip angle of 30° was used throughout the study. The slice thickness was 1 mm, and the numbers of slices were 17 to 20, which was sufficient to cover the entire lung. The acquisition matrix size was 256 × 128, the reconstructed matrix size was 256 × 256, and the field of view was 2.56 × 2.56 cm². Motion artifacts were minimized by application of cardiac and respiratory gating to all MRI studies. All animals were scanned using the described settings and parameters. Tumor volume (mm³) per animal was quantified by manual segmentation of the visible lung opacities present in each axial image sequence (a maximum of 10 consecutive scans were evaluated per mouse) to calculate tumor volumes using 3D Slicer (version 3.6.3) as described previously (41).

Immunohistochemistry

All samples were harvested for histology analysis at endpoint unless otherwise specified. Samples resected from mice were fixed overnight in formalin, and then stored in 70% EtOH before processing and embedding. Immunohistochemistry was conducted on 5 μm/L sections. Tissue sections were deparaffinized, rehydrated, and boiled for 15 minutes with a pressure cooker in 10 mmol/L pH 6.0 Citrate buffer. Slides were incubated in 3% hydrogen peroxide for 30 minutes and then blocked in serum for 1 hour. Primary antibody was added to the section and incubated overnight at 4°C. Sections were further incubated with biotin-conjugated secondary antibody for 1 hour and Avidin-Biotin Complexes for 30 minutes (Vector Laboratories) and developed by 3,3'-diaminobenzidine following by hematoxylin staining. After staining, the sections were dehydrated and mounted in permount mounting medium (SP15-100; Fisher Scientific). Primary antibody and dilution used were as follows: RFP rabbit polyclonal (1:500, 600-401-379); Cleaved Caspase-3 rabbit polyclonal (1:200, D175; Cell Signaling Technology); Ki67 rabbit polyclonal (1:100, clone K2; Ventana Medical Systems); CK19 (1:50, DSHB; University of Iowa, IA); Insulin (1:500, 3014S; Cell signaling Technology); Amylase (1:1,000, Sigma; MO); CD68 mouse monoclonal (1:200, Kp-1; Cell Marque); CD3 (1:500, Cell Marque); Desmin (1:200, cloneD33; Dako); and LC3 (1:500, NBP-19167; Novus Biologicals). Images were taken using light Microscope Leica DM2000 with camera. LC3 staining was modified with additional steps using TSA biotin system following the manufacturer's instructions (NEL700A001KT; PerkinElmer). Arginase 1 (1:100, NBP1-32731; Novus Biological)–stained IHC slides were scanned with 20x objective using Leica SCN400F whole-slide scanner, the DAB and hematoxylin-stained areas were calculated using ImageJ and analyzed using GraphPad Prism 7.03.

Immunofluorescence

Cells were grown on round coverslips in 12-well plate and fixed with 4% formaldehyde for 15 minutes. Fixed cells were blocked with

5% BSA/0.3% Triton X-100 in PBS for 1 hour, and then incubated with primary antibody diluted in 1% BSA/0.3% Triton X-100 in PBS overnight at 4°C. After being incubated with fluorochrome-conjugated secondary antibody for 1 hour at room temperature in the dark, cells were mounted in ProLong Gold antifade mounting medium DAPI (P36931; ThermoFisher). Images were taken with 6 channel fluorescent microscope Nikon Eclipse 80i with camera.

F4/80 and iNOS IF were performed on tumor sections: F4/80 (1:400, MCA497GA, Cl:A3-1; Bio-Rad), iNOS (1:600, LS-C88790/110398; LSBio), and DAPI (D1306; ThermoFisher). IF was performed using Opal 4-color manual IHC kit (NEL810001KT, PerkinElmer) following the manufacturer's protocol. Images with F4/80+ signals were taken with 40x objective using Leica DM6B. The ratio of total area of fluorescence was calculated and normalized with the total area of DAPI using ImageJ.

Western

Proteins were extracted with RIPA buffer and separated on 4% to 12% stacking SDS-PAGE gel, and then transferred to PVDF membrane (Bio-Rad). Membranes were blocked with 5% nonfat milk and then incubated with the primary antibody overnight at 4°C. Following TBST washing, membranes were incubated with peroxidase-conjugated secondary antibody for 1 hour and exposed on film using the enhanced chemiluminescence detection system (Thermo Scientific). Antibodies used were as follows: RFP rabbit polyclonal (1:1,000, 600-401-379); Cleaved Caspase-3 rabbit polyclonal (1:500, D175; Cell Signaling Technology); LC3B (1:500, NB600-1384; Novus Biological), and β-actin (1:3,000, A2066; Sigma).

Serum Insulin Measurement

Serum was collected at harvest, where whole blood was allowed to clot. Then after centrifugation, the supernatant was carefully collected, aliquot, and stored in -80°C. Insulin level was measured using mouse insulin Elisa kit (10-1247-01; Merckodia) following the manufacturer's instructions.

Colony Assay

Cells were pretreated with or without Dox for 7 days before plating into 6-well plates. A total of 500 cells per well were plated in growth medium with 10% FBS with or without 2 μg/mL Dox. After 6 days, cells were fixed in 80% methanol and stained with 0.2% crystal violet, and colonies were counted. The surviving fraction was calculated using the plating efficiency.

Soft-Agar Assay

Each cell line was plated in triplicate in 6-well plate. Note that 3 mL medium with 1% agar (Difco 214200; BD) was used as bottom gel. After the bottom layer solidified, 10⁴ cells suspended in 2 mL medium with 0.4% agar were poured on bottom gel. After 2 weeks, colonies were stained with p-iodonitrotetrazonium violet (I-8377; Sigma). Number of colonies was counted from pictures taken at low power lens of microscopy. Size of colonies was analyzed by ImageJ software.

Cell Culture

All cell lines used in the study were primary PDAC lines derived from mouse primary tumors and grown in RPMI-1640 (11875, Thermo Fisher) with 10% FBS and 1% Penstrip, and were derived during the last 2 years. Mice were genotyped to confirm the correct alleles for cell line derivation. Cell cultures were maintained in a humidified incubator at 37°C with 5% CO₂. All primary tumor cell lines were harvested from approximately 5 mm³ chunk of tumor, minced and digested in 4% collagenase/dispase for 1 hour, and then filtered through a 70-μm restrainer. Cell lines were routinely tested and all were

negative for *Mycoplasma* infection. Inducibility and presence of the ATG4b dominant negative were tested by adding Dox to culture media.

Orthotopic Injection

Primary tumor cell lines were harvested from tumor-bearing naïve mice at a B6/FVB mix background. Haplotype of each cell line was identified according to their MHC II loci by PCR analysis as described in refs. 42, 43. Because host mice were all F1 from B6 (*Ubc-ERT/Cre⁺*) and FVB/N (*Atg4B^{CA++}*, *Rosa-rtTA^{LSL}*) crosses, we used cell lines carrying both B6 haplotype MHC2^b and FVB/N haplotype MHC2^a to minimize allograft rejection. Mice were anesthetized by intraperitoneal injection of ketamine (10 mg/mL)/xylazine (1 mg/mL) cocktail at the ratio of 10 μ L cocktail per 1 g body weight. After local shaving and disinfection, the upper left abdominal cavity was opened by a 1 cm-long incision. The spleen was pulled to expose the tail of the pancreas. Ice-cold tumor cells (10 μ L; 3×10^5) mixed with Matrigel (1:1) were then slowly injected into the pancreas using an ice-cold 22-gauge Hamilton syringe (20736; Sigma). To prevent leakage, a bubble needed to be visible at the injection site, and the needle was not removed for 15 seconds. After injection, the abdominal cavity was closed with absorbptive suture and stainless-steel staples. Mice were given buprenorphine to alleviate pain after surgery and monitored following protocol.

Ultrasound screening was used for tumor seeding efficiency assessment starting 1 week after injection. Lesion with diameter over 2 mm was denoted as successful seeding. For mice with positive seeding, tumor growth was followed up to 4 weeks.

Xenograft

Primary mouse tumor cells (10^5) were suspended in PBS, mixed with Matrigel (BD Biosciences) at a 1:1 ratio, and subcutaneously injected into nude female mice (Nu/Nu; Charles River Laboratories) in a final volume of 100 μ L. Each mouse was inoculated with ATG4B⁻ cells on the left flank and ATG4B^{CA++} cells on the right flank. Ten mice were kept on normal diet, and 10 mice were kept on Dox diet 1 week after injection when tumors reached volumes of 40 mm³. Tumor length and width were measured twice a week using caliper. The volumes of tumor were calculated using the formula ($L \times W^2$)/2.

Electron Microscopy

Tumors were fixed with Karnovsky fixative (15732-SP; Electron Microscopy Sciences). Embedding, sectioning, and staining were done in the Harvard Medical School EM Facility. The EM pictures were captured by a conventional transmission electron microscope (JEOL 1200EX) equipped with an AMT 2k CCD camera.

Immune Profiling

Spleen and pancreatic tumors were harvested from tumor-bearing mice, minced in 3 mL lysis buffer (HBSS + 50 U/mL DnaseI + 0.5 mg/mL Collagenase D + 2.5 mmol/L MgCl₂), and incubated at 37°C for 30 minutes. Tissue chunks were ground with a rubber grinder and passed through a 70- μ m cell restrainer. Cells were incubated with 5 mL 1x RBC lysis buffer (420301; BioLegend) for 4 minutes, then diluted in 2% FBS in 1x PBS to a final volume of 30 mL, and spun down. Live cells were determined by LIVE/DEAD fixable aqua dead cell stain kit (Molecular Probes). The cell pellets were resuspended in PBS with 2% FBS for FACS analysis. Cells were stained with cell surface markers as indicated followed by fixation/permeabilization using a FOXP3 fixation/permeabilization kit (eBioscience). Cells were imaged on BD LSRFortessa (BD Biosciences) and analyzed using FlowJo software (Tree Star). Pancreas infiltrating immune cells were stained with different combinations of fluorochrome-coupled antibodies against mouse CD45 (clone 30-F11; BioLegend) and F4/80 (clone BM8; BioLegend).

Depletion of Macrophage

Clodronate liposomes/PBS control liposomes were purchased from www.clodronateliposomes.com. Doses injected were calculated based on the weight of mice to be treated at a ratio of 10 μ L per 1 g body weight (e.g., 200 μ L liposome for 20 g mouse). Once a tumor-bearing mouse was identified, it was assigned to clodronate or PBS liposome groups in an alternating fashion. First dose of clodronate or PBS liposome was administered on the same day the tumor was identified, and following doses were given twice a week.

Statistical Analysis

Overall survival events included death as defined by protocol with censoring for alive at last follow-up. Survival plots were generated using the Kaplan–Meier method. The log-rank test was used to compare survival distributions between groups. The seeding efficiency of mice with orthotopic injection was compared using a Fisher exact test. Statistical analyses were performed using Prism 7 (GraphPad Software).

Disclosure of Potential Conflicts of Interest

A.C. Kimmelman has ownership interest (including patents) in Vescor Therapeutics and Rafael Pharmaceuticals, and is a consultant/advisory board member for Astellas and Forma Therapeutics. No potential conflicts of interest were disclosed by the other authors.

Authors' Contributions

Conception and design: A. Yang, K.-K. Wong, A.C. Kimmelman
Development of methodology: A. Yang, G. Herter-Sprie, E.Y. Lin
Acquisition of data (provided animals, acquired and managed patients, provided facilities, etc.): A. Yang, G. Herter-Sprie, H. Zhang, X. Wang, J. Deng, J. Hai, S. Yang, K.-K. Wong
Analysis and interpretation of data (e.g., statistical analysis, biostatistics, computational analysis): A. Yang, G. Herter-Sprie, H. Zhang, E.Y. Lin, J. Deng, J. Hai, K.-K. Wong
Writing, review, and/or revision of the manuscript: A. Yang, G. Herter-Sprie, H. Zhang, E.Y. Lin, K.-K. Wong, A.C. Kimmelman
Administrative, technical, or material support (i.e., reporting or organizing data, constructing databases): A. Yang, H. Zhang, E.Y. Lin, D. Biancur, A.C. Kimmelman
Study supervision: H. Zhang, E.Y. Lin, D. Biancur, A.C. Kimmelman

Acknowledgments

This work was supported by National Cancer Institute Grants R01CA157490, R01CA188048 (to A.C. Kimmelman), and P01CA117969 (subaward to A.C. Kimmelman); ACS Research Scholar Grant RSG-13-298-01-TBG (to A.C. Kimmelman); NIH grant R01GM095567 (to A.C. Kimmelman); and the Lustgarten Foundation (to A.C. Kimmelman).

Received August 22, 2017; revised December 5, 2017; accepted January 2, 2018; published OnlineFirst January 9, 2018.

REFERENCES

- Abrams MJ, Rakaszowski K, Vasekar M, Passero F, Abbas A, Jia Y, et al. Recent advances in pancreatic cancer: updates and insights from the 2015 Annual Meeting of the American Society of Clinical Oncology. *Therap Adv Gastroenterol* 2016;9:141–51.
- Yang S, Wang X, Contino G, Liesa M, Sahin E, Ying H, et al. Pancreatic cancers require autophagy for tumor growth. *Genes Dev* 2011;25:717–29.
- Rosenfeldt MT, O'Prey J, Morton JP, Nixon C, MacKay G, Mrowinska A, et al. p53 status determines the role of autophagy in pancreatic tumour development. *Nature* 2013;504:296–300.

4. Yang A, Rajeshkumar NV, Wang X, Yabuuchi S, Alexander BM, Chu GC, et al. Autophagy is critical for pancreatic tumor growth and progression in tumors with p53 alterations. *Cancer Discov* 2014;4:905–13.
5. White E. Deconvoluting the context-dependent role for autophagy in cancer. *Nat Rev Cancer* 2012;12:401–10.
6. Kimmelman AC, White E. Autophagy and tumor metabolism. *Cell Metab* 2017;25:1037–43.
7. Yang A, Kimmelman AC. Inhibition of autophagy attenuates pancreatic cancer growth independent of TP53/TRP53 status. *Autophagy* 2014;10:1683–4.
8. Guo JY, White E. Autophagy is required for mitochondrial function, lipid metabolism, growth, and fate of KRAS(G12D)-driven lung tumors. *Autophagy* 2013;9:1636–8.
9. Katheder NS, Khezri R, O'Farrell F, Schultz SW, Jain A, Rahman MM, et al. Microenvironmental autophagy promotes tumour growth. *Nature* 2017;541:417–20.
10. Sousa CM, Biancur DE, Wang X, Halbrook CJ, Sherman MH, Zhang L, et al. Pancreatic stellate cells support tumour metabolism through autophagic alanine secretion. *Nature* 2016;536:479–83.
11. Xie X, Koh JY, Price S, White E, Mehnert JM. Atg7 overcomes senescence and promotes growth of BrafV600E-driven melanoma. *Cancer Discov* 2015;5:410–23.
12. Huo Y, Cai H, Teplova I, Bowman-Colin C, Chen G, Price S, et al. Autophagy opposes p53-mediated tumor barrier to facilitate tumorigenesis in a model of PALB2-associated hereditary breast cancer. *Cancer Discov* 2013;3:894–907.
13. Guo JY, Karsli-Uzunbas G, Mathew R, Aisner SC, Kamphorst JJ, Strohecker AM, et al. Autophagy suppresses progression of K-ras-induced lung tumors to oncocytomas and maintains lipid homeostasis. *Genes Dev* 2013;27:1447–61.
14. Shchors K, Massaras A, Hanahan D. Dual targeting of the autophagic regulatory circuitry in gliomas with repurposed drugs elicits cell-lethal autophagy and therapeutic benefit. *Cancer Cell* 2015;28:456–71.
15. Santanam U, Banach-Petrosky W, Abate-Shen C, Shen MM, White E, DiPaola RS. Atg7 cooperates with Pten loss to drive prostate cancer tumor growth. *Genes Dev* 2016;30:399–407.
16. Karsli-Uzunbas G, Guo JY, Price S, Teng X, Laddha SV, Khor S, et al. Autophagy is required for glucose homeostasis and lung tumor maintenance. *Cancer Discov* 2014;4:914–27.
17. Wolpin BM, Rubinson DA, Wang X, Chan JA, Cleary JM, Enzinger PC, et al. Phase II and pharmacodynamic study of autophagy inhibition using hydroxychloroquine in patients with metastatic pancreatic adenocarcinoma. *Oncologist* 2014;19:637–8.
18. Rangwala R, Chang YC, Hu J, Algazy KM, Evans TL, Fecher LA, et al. Combined MTOR and autophagy inhibition: phase I trial of hydroxychloroquine and temsirolimus in patients with advanced solid tumors and melanoma. *Autophagy* 2014;10:1391–402.
19. Rangwala R, Leone R, Chang YC, Fecher LA, Schuchter LM, Kramer A, et al. Phase I trial of hydroxychloroquine with dose-intense temozolomide in patients with advanced solid tumors and melanoma. *Autophagy* 2014;10:1369–79.
20. Vogl DT, Stadtmayer EA, Tan KS, Heitjan DF, Davis LE, Pontiggia L, et al. Combined autophagy and proteasome inhibition: a phase I trial of hydroxychloroquine and bortezomib in patients with relapsed/refractory myeloma. *Autophagy* 2014;10:1380–90.
21. Perera RM, Stoykova S, Nicolay BN, Ross KN, Fitamant J, Boukhali M, et al. Transcriptional control of autophagy-lysosome function drives pancreatic cancer metabolism. *Nature* 2015;524:361–5.
22. Amaravadi RK, Yu D, Lum JJ, Bui T, Christophorou MA, Evan GI, et al. Autophagy inhibition enhances therapy-induced apoptosis in a Myc-induced model of lymphoma. *J Clin Invest* 2007;117:326–36.
23. Rebecca VW, Amaravadi RK. Emerging strategies to effectively target autophagy in cancer. *Oncogene* 2016;35:1–11.
24. Boone BA, Bahary N, Zureikat AH, Moser AJ, Normolle DP, Wu WC, et al. Safety and biologic response of pre-operative autophagy inhibition in combination with gemcitabine in patients with pancreatic adenocarcinoma. *Ann Surg Oncol* 2015;22:4402–10.
25. Miller-Ocuin JL, Bahary NS, Singhi AD, Normolle DP, Lembersky B, Stoller R, et al. Inhibition of autophagy improves pathologic and biomarker response to preoperative gemcitabine/nab-paclitaxel in potentially resectable pancreatic cancer: a phase II randomized controlled trial. *Ann Surg Oncol* 2017;24:S6–S7.
26. Fujita N, Hayashi-Nishino M, Fukumoto H, Omori H, Yamamoto A, Noda T, et al. An Atg4B mutant hampers the lipidation of LC3 paralogs and causes defects in autophagosome closure. *Mol Biol Cell* 2008;19:4651–9.
27. Feig C, Gopinathan A, Neece A, Chan DS, Cook N, Tuveson DA. The pancreas cancer microenvironment. *Clin Cancer Res* 2012;18:4266–76.
28. Beatty GL, Chiorean EG, Fishman MP, Saboury B, Teitelbaum UR, Sun W, et al. CD40 agonists alter tumor stroma and show efficacy against pancreatic carcinoma in mice and humans. *Science* 2011;331:1612–6.
29. Beard C, Hochedlinger K, Plath K, Wutz A, Jaenisch R. Efficient method to generate single-copy transgenic mice by site-specific integration in embryonic stem cells. *Genesis* 2006;44:23–8.
30. Mulcahy Levy JM, Zahedi S, Griesinger AM, Morin A, Davies KD, Aisner DL, et al. Autophagy inhibition overcomes multiple mechanisms of resistance to BRAF inhibition in brain tumors. *eLife* 2017;6.
31. Kimmelman AC. The dynamic nature of autophagy in cancer. *Genes Dev* 2011;25:1999–2010.
32. Gross MI, Demo SD, Dennison JB, Chen L, Chernov-Rogan T, Goyal B, et al. Antitumor activity of the glutaminase inhibitor CB-839 in triple-negative breast cancer. *Mol Cancer Ther* 2014;13:890–901.
33. Brown JM, Recht L, Strober S. The promise of targeting macrophages in cancer therapy. *Clin Cancer Res* 2017;23:3241–50.
34. Lock R, Kenific CM, Leidal AM, Salas E, Debnath J. Autophagy-dependent production of secreted factors facilitates oncogenic RAS-driven invasion. *Cancer Discov* 2014;4:466–79.
35. Premrurit PK, Dow LE, Kim SY, Camiolo M, Malone CD, Miething C, et al. A rapid and scalable system for studying gene function in mice using conditional RNA interference. *Cell* 2011;145:145–58.
36. Belteki G, Haigh J, Kabacs N, Haigh K, Sison K, Costantini F, et al. Conditional and inducible transgene expression in mice through the combinatorial use of Cre-mediated recombination and tetracycline induction. *Nucleic Acids Res* 2005;33:e51.
37. Jackson EL, Willis N, Mercer K, Bronson RT, Crowley D, Montoya R, et al. Analysis of lung tumor initiation and progression using conditional expression of oncogenic K-ras. *Genes Dev* 2001;15:3243–8.
38. Jonkers J, Meuwissen R, van der Gulden H, Peterse H, van der Valk M, Berns A. Synergistic tumor suppressor activity of BRCA2 and p53 in a conditional mouse model for breast cancer. *Nat Genet* 2001;29:418–25.
39. Kawaguchi Y, Cooper B, Gannon M, Ray M, MacDonald RJ, Wright CV. The role of the transcriptional regulator Ptf1a in converting intestinal to pancreatic progenitors. *Nat Genet* 2002;32:128–34.
40. Ruzankina Y, Pinzon-Guzman C, Asare A, Ong T, Pontano L, Cotterelli G, et al. Deletion of the developmentally essential gene ATR in adult mice leads to age-related phenotypes and stem cell loss. *Cell Stem Cell* 2007;1:113–26.
41. Herter-Sprue GS, Korideck H, Christensen CL, Herter JM, Rhee K, Berbeco RI, et al. Image-guided radiotherapy platform using single nodule conditional lung cancer mouse models. *Nat Commun* 2014;5:5870.
42. Saha BK. Typing of murine major histocompatibility complex with a microsatellite in the class II Eb gene. *J Immunol Methods* 1996;194:77–83.
43. Takeuchi Y, Watanabe S, Ishii G, Takeda S, Nakayama K, Fukumoto S, et al. Interleukin-11 as a stimulatory factor for bone formation prevents bone loss with advancing age in mice. *J Biol Chem* 2002;277:49011–8.